Published in final edited form as:
Comput Methods Appl Mech Eng. 2017 June 15; 320: 352–368. doi:10.1016/j.cma.2017.03.015.

The importance of mechano-electrical feedback and inertia in cardiac electromechanics

Francisco Sahli Costabal[a], **Felipe A. Concha**[b], **Daniel E. Hurtado**[b,c], and **Ellen Kuhl**[d]

[a]Department of Mechanical Engineering, Stanford University, Stanford, CA 94305, USA

[b]Department of Structural and Geotechnical Engineering, School of Engineering, Pontificia Universidad Católica de Chile, Santiago, Chile

[c]Institute for Biological and Medical Engineering, Schools of Engineering, Medicine and Biological Sciences, Pontificia Universidad Catoólica de Chile, Santiago, Chile

[d]Departments of Mechanical Engineering, Bioengineering, and Cardiothoracic Surgery, Stanford University, Stanford, CA 94305, USA

Abstract

In the past years, a number cardiac electromechanics models have been developed to better understand the excitation-contraction behavior of the heart. However, there is no agreement on whether inertial forces play a role in this system. In this study, we assess the influence of mass in electromechanical simulations, using a fully coupled finite element model. We include the effect of mechano-electrical feedback via stretch activated currents. We compare five different models: electrophysiology, electromechanics, electromechanics with mechano-electrical feedback, electromechanics with mass, and electromechanics with mass and mechano-electrical feedback. We simulate normal conduction to study conduction velocity and spiral waves to study fibrillation. During normal conduction, mass in conjunction with mechano-electrical feedback increased the conduction velocity by 8.12% in comparison to the plain electrophysiology case. During the generation of a spiral wave, mass and mechano-electrical feedback generated secondary wavefronts, which were not present in any other model. These secondary wavefronts were initiated in tensile stretch regions that induced electrical currents. We expect that this study will help the research community to better understand the importance of mechanoelectrical feedback and inertia in cardiac electromechanics.

Keywords

Electro-mechanics; Excitation-contraction; Cardiac mechanics; Finite element analysis; Abaqus

---

1. Motivation

The heart is composed of four chambers and its primary function is to circulate blood in the cardivascular system. To achieve this goal, electrical waves travel through the cardiac tissue to trigger muscle contraction and generate a coordinated movement of the ventricles that pump blood through the arteries. Despite tremendous scientific advances, heart disease is responsible for half a million deaths each year in the United States alone [39]. Many of these deaths are caused by lethal arrhythmias, which provoke an abnormal electrical activity of the heart that ultimately leads to mechanical dysfunction and death. In the case of cardiac fibrillation, arrhythmias are driven by electrical spiral waves that self-excite, preventing the coordinated contraction of cardiac tissue and diminishing the pumping capacity of the heart [45]. The electrical wave that modulates muscle contraction is influenced by the mechanical deformation. Indeed, mechanical contraction deforms the domain where the electrical wave is propagating, altering wave dynamics. Moreover, transmembrane currents are generated by the stretching of ionic channels. This mechano-electrical feedback is thought to be responsible for “commotio cordis”, a condition in which the precordial impact of an object may start ventricular fibrillation [33]. Mechano-electrical feedback is also responsible for “precordial thump”, a procedure in which the currents generated by this mechanism are used to stop fibrillation [7].

Computational modeling can help to better understand the interplay between the electrical and the mechanical behavior in the heart, that would otherwise be difficult to characterize in laboratory experiments [8, 37]. Given the complexity of these interactions, different computational studies decide to include or neglect certain components of the electromechanical system. For example, most electrophysiology simulations are performed on a fixed domain, ignoring the mechanical interaction [48, 2, 14, 11]. When the focus is on the mechanical aspects of the tissue, the influence of deformation over the electric field is not directly adressed, as the electrical and mechanical models are solved separately [50, 4]. An intermediate approach is to solve the electrical and mechanical problems staggered [53, 41, 32, 43, 29]. Another component that is often neglected is the inertia term in the balance of linear momentum. Although some studies include the influence of mass in simulations of the heart [54, 9, 51], a large majority neglects its influence [10, 41, 43, 32, 31, 5]. In this work, we explore the effect of inertia in electromechanical models. We hypothesize that additional deformations caused by inertia may alter the electrical wave dynamics via the mechano-electrical feedback. Using our fully coupled formulation [18], we assess the influence of mass in normal wave propagation and in the case of fibrillation by simulating a spiral wave. We measure electrophysiological variables including the conduction velocity and the spiral wave trajectory. We also asses the influence of mechano-electrical feedback currents and their relation with inertial effects. To our knowledge, this is the first study to systematically quantify the inertial effect in a three-dimensional electromechanical model.

This manuscript is organized as follows: Section 2 covers the continuum formulation of the electromechanics problem, Section 3 describes the computational implementation, Section 4 describes the particular models we use to study conduction velocity and spiral waves along with the results of these studies. We conclude with a critical discussion in Section 5.

2. Continuum eletromechanical model

We illustrate the continuum model of electro-mechanical coupling by briefly summarizing the kinematic equations, the balance equations, and the constitutive equations of excitation-contraction coupling.

2.1. Kinematic equations

To characterize the kinematics of finite deformation, we introduce the deformation map $\boldsymbol{\varphi}$, which maps particles $\boldsymbol{X}$ from the undeformed material configuration $\mathscr{B}_0 \subset \mathbb{R}^3$ to particles $\boldsymbol{x} = \boldsymbol{\varphi}(X, t)$ in the deformed spatial configuration $\mathscr{B}=\varphi_t\left(\mathscr{B}_0\right) \subset \mathbb{R}^3$ [24]. Its derivative with respect to the undeformed coordinates $\boldsymbol{X}$ defines the deformation gradient,

$$\boldsymbol{F}=\nabla\varphi, \quad (1)$$

from which we characterize local volume changes by computing the Jacobian $J = \det(\boldsymbol{F})$. We further introduce the right Cauchy-Green deformation tensor,

$$\boldsymbol{C}=\boldsymbol{F}^{\mathrm{t}} \cdot \boldsymbol{F}, \quad (2)$$

and consider the invariants,

$$I_3=\det\left(\boldsymbol{C}\right)=\det^2\left(\boldsymbol{F}\right)=J^2 \text{ and } I_4=\boldsymbol{C}\colon[\boldsymbol{f}_0 \otimes \boldsymbol{f}_0]=\boldsymbol{f} \cdot \boldsymbol{f}=\lambda^2, \quad (3)$$

where $\boldsymbol{f}_0$ is the material myocardial fiber unit vector, $\boldsymbol{f} = \boldsymbol{F}\cdot\boldsymbol{f}_0$ is the spatial myocardial fiber vector with norm $\lambda=\sqrt{\boldsymbol{f}\cdot\boldsymbol{f}}$, and : represents the tensor contraction operator. The invariant I_3 quantifies volumetric changes and the invariant I_4 quantifies the cardiac fiber stretch. We further introduce the spatial myocardial fiber unit vector $\hat{\boldsymbol{f}}=\boldsymbol{f}/\lambda$. In what follows, we denote the material time derivative as $\{\dot{\circ}\}=d\{\circ\}/\mathrm{d}t$ and the material gradient and divergence as $\nabla\{\circ\} = \partial\{\circ\}/\partial\boldsymbol{X}$ and $\mathrm{Div}\,\{\circ\} = \partial\{\circ\}/\partial\boldsymbol{X} : \boldsymbol{I}$ and the spatial gradient as $\nabla_{\boldsymbol{x}}\{\circ\} = \partial\{\circ\}/\partial\boldsymbol{x}$.

2.2. Balance equations

We characterize the electrical problem through the normalized monodomain equation for the transmembrane potential $\Phi\colon\mathscr{B}_0 \times \mathbb{R} \rightarrow \mathbb{R}$ and define the mechanical problem through the balance of linear momentum for the deformation $\boldsymbol{\varphi}$,

$$\begin{gathered}\dot{\Phi}=\mathrm{Div}\,\left(\boldsymbol{Q}\right)+F^{\Phi} \;\; in\ \mathscr{B}_0 \times \mathbb{R} \\ \rho_0\ddot{\varphi}=\mathrm{Div}\left(\boldsymbol{F}\cdot\boldsymbol{S}\right)+\boldsymbol{F}^{\varphi} \;\; in\ \mathscr{B}_0 \times \mathbb{R}.\end{gathered} \quad (4)$$

Here, $\boldsymbol{Q}$ is the material electrical flux, $\boldsymbol{F}^{\Phi}$ is the material ionic current, ρ_0 is the material density, $\boldsymbol{S}$ is the second Piola-Kirchhoff stress, and $\boldsymbol{F}^{\varphi}$ is the external mechanical force vector. We note that the deformation mapping allow us to compute the spatial transmembrane potential $\phi:\mathscr{B}\times\mathbb{R}\to\mathbb{R}$ through mapping composition, i.e. $\boldsymbol{\phi}(\boldsymbol{x},t) = \boldsymbol{\Phi}(\boldsymbol{\varphi}^{-1}(\boldsymbol{x},t),t)$.

2.3. Constitutive equations

To close the set of equations, we specify the constitutive equations for the electrical flux $\boldsymbol{Q}$, the ionic current F^{Φ}, the second Piola-Kirchhoff stress $\boldsymbol{S}$, and the external forces $\boldsymbol{F}^{\varphi}$ Following Fick's law, we assume that the electrical flux proportional to the gradient of the transmembrane potential in the spatial configuration,

$$\boldsymbol{q}=-\boldsymbol{d}\cdot\nabla_{\boldsymbol{x}}\phi, \qquad (5)$$

where $\boldsymbol{d}=d^{\text{iso}}\boldsymbol{I}+d^{\text{ani}}\hat{\boldsymbol{f}}\otimes\hat{\boldsymbol{f}}$ denotes the conductivity tensor, which consists of an isotropic contribution d^{iso} and an anisotropic contribution d^{ani} to account for faster conductivity along the current fiber direction $\hat{\boldsymbol{f}}$ [12]. Using the Piola transform $\boldsymbol{Q} = \boldsymbol{F}^{-1}\,\boldsymbol{q}/J$, we express the material electrical flux,

$$\boldsymbol{Q}=-\boldsymbol{D}\cdot\nabla\Phi, \qquad (6)$$

where $\boldsymbol{D} = D^{\text{iso}}\,\boldsymbol{C}^{-1} + D^{\text{ani}}\boldsymbol{f}_0\otimes\boldsymbol{f}_0/\lambda^2$ is the conductivity tensor in the material configuration. The material and spatial conductivity parameters are related as $D^{\text{iso}} = J\,d^{\text{iso}}$ and $D^{\text{ani}} = J\,d^{\text{ani}}$. For the ionic current, we consider a purely electrochemical component F_{e}^{Φ} plus a mechano-electrical feedback component F_{m}^{Φ},

$$F^{\Phi}=F_{\text{e}}^{\Phi}+F_{\text{m}}^{\Phi}. \qquad (7)$$

For the purely electrochemical component, we adopt a modified version of the Aliev-Panfilov model for ionic current [2, 27, 49],

$$F_{\text{e}}^{\Phi}=c_1\Phi\,[\Phi-\alpha]\,[\Phi-1]-c_2\,r\,\Phi, \qquad (8)$$

where the cubic polynomial term controls the fast upstroke of the action potential through the parameters c_2 and α [15, 40], and the coupling term controls the slow repolarization through the recovery variable r [2]. We treat the recovery variable as an internal variable, which evolves according to the kinetic equation,

$$\dot{r}=[\gamma+r\mu_1/[\mu_2+\Phi]]\,[-r-c_2\Phi\,[\Phi-b-1]], \qquad (9)$$

where the recovery parameters γ, μ_1,μ_2 and b control the restitution behavior [2]. The mechano-electrical feedback reflects the effects of ionic current of stretch-activated ion channels, which we assume to the proportional to the stretch in fiber direction [18, 43, 54],

$$F_{\mathrm{m}}^{\Phi}=G_{\mathrm{s}}\theta\left[\lambda-1\right]\left[\Phi_{\mathrm{s}}-\Phi\right]. \quad (10)$$

Here, Φ_{s} is the resting potential of this current and $\theta(\lambda)$ with $\theta(\lambda) = 0$ for $\lambda < 1$ and $\theta(\lambda) = 1$ for $\lambda \geq 1$ is a step function that only activates this current in tension. Finally, we map the resulting fields and source terms into the physiological domain via $\hat{\Phi}=100\Phi-80mV$ and $\tau = 12.9\ t$ ms, to create physiologically realistic transmembrane potentials $\hat{\Phi}$ that range from −80 mV to +20 mV.

For simplicity, we do not consider a kinematic approach towards active muscle contraction in the sense of the generalized Hill model [19], but rather follow the standard Hill model in which the tissue stress consists of passive and active contributions,

$$\boldsymbol{S}=\boldsymbol{S}^{\mathrm{pas}}+\boldsymbol{S}^{\mathrm{act}}. \quad (11)$$

For the passive stress, we assume a nearly incompressible, fiber reinforced, neo-Hookean behavior [17],

$$\boldsymbol{S}^{\mathrm{pas}}=\frac{1}{2}\left[\lambda\, ln\left(I_3\right)-2\mu\right]\boldsymbol{C}^{-1}+\mu\boldsymbol{I}+2\eta\theta\left[I_4-1\right]\boldsymbol{f}_0\otimes\boldsymbol{f}_0. \quad (12)$$

The parameters λ and μ are the Lamé constants, η controls the stiffness in the fiber direction, and θ activates the fiber stiffness only in the case of fiber tension, i.e., $\lambda \geq 1$. For the active stress, we assume that contraction acts primarily along the fiber direction $\boldsymbol{f}_0$,

$$\boldsymbol{S}^{\mathrm{act}}=T^{\mathrm{act}}I_4^{-1}\,\boldsymbol{f}_0\otimes\boldsymbol{f}_0\ \text{ with }\ \dot{T}^{\mathrm{act}}=\varepsilon\left(\Phi\right)\left[k_T\left[\Phi-\Phi_{\mathrm{r}}\right]-T^{\mathrm{act}}\right]. \quad (13)$$

In this model, the active muscle traction T^{act} is driven by changes in the electrical potential and the parameters k_T and Φ_{r} control the maximum active force and the resting potential [41]. The activation function, $\varepsilon=\varepsilon_0+\left[\varepsilon_\infty-\varepsilon_0\right]exp\left(-exp\left(-\xi\left[\Phi-\overline{\Phi}\right]\right)\right)$, ensures a smooth activation of the muscle traction T^{act} in terms of the limiting values ε_0 at $\Phi \to -\infty$ and and ε_∞ at at $\Phi \to +\infty$, the phase shift $\overline{\Phi}$, and the transition slope ξ [18]. In the following, we consider the case of no external forces and set $\boldsymbol{F}^{\varphi} = \boldsymbol{0}$.

3. Computational model

In this section, we illustrate the finite element discretization of the governing equations, demonstrate their consistent linearization, discuss the handling of their internal variables [6] and present the most relevant sensitivities.

3.1. Strong and weak forms

To derive the weak form of the governing equations, we reformulate the electrical and mechanical balance equations (4) in their residual forms and introduce the electrical and mechanical residuals R^{Φ} and $\mathbf{R}^{\varphi}$ throughout the entire cardiac domain $\mathscr{B}_0$.

$$\begin{aligned}\mathrm{R}^{\Phi} &= \dot{\Phi} - \mathrm{Div}\,(\boldsymbol{Q}) - F^{\Phi} \doteq 0\\ \mathbf{R}^{\varphi} &= \rho_0\,\ddot{\varphi} - \mathrm{Div}\,(\boldsymbol{F}\cdot\boldsymbol{S}) - \boldsymbol{F}^{\varphi} \doteq \mathbf{0}.\end{aligned} \qquad (14)$$

We prescribe Dirichlet boundary conditions $\Phi = \overline{\Phi}$ and $\varphi = \overline{\varphi}$ on the Dirichlet boundary and Neumann boundary conditions $\boldsymbol{Q}\cdot\boldsymbol{N} = \overline{t}^{\Phi}$ and $\boldsymbol{F}\cdot\boldsymbol{S}\cdot\boldsymbol{N} = \overline{\boldsymbol{t}}^{\varphi}$ on the Neumann boundary with outward normal $\boldsymbol{N}$. For simplicity, we assume homogeneous Neumann boundary conditions, i.e., $\overline{t}^{\Phi} = 0$ and $\overline{\mathbf{t}}^{\varphi} = \mathbf{0}$. We multiply the residuals (14) by the scalar- and vector-valued test functions, $\delta\Phi$ and $\delta_{\boldsymbol{\varphi}}$, integrate them over the domain $\mathscr{B}_0$, and integrate the flux terms by parts to obtain the weak forms of the electrical and mechanical problems,

$$\begin{aligned}\mathrm{G}^{\Phi} &= \int_{\mathscr{B}_0} \delta\Phi\ \dot{\Phi}\,\mathrm{d}v + \int_{\mathscr{B}_0} \nabla\delta\Phi\cdot\boldsymbol{Q}\ \mathrm{d}V - \int_{\mathscr{B}_0} \delta\,\Phi\, F^{\Phi}\,\mathrm{d}V \doteq 0\\ \mathrm{G}^{\varphi} &= \int_{\mathscr{B}_0} \delta\varphi\cdot\rho_0\ddot{\boldsymbol{\varphi}}\,\mathrm{d}V + \int_{\mathscr{B}_0} \nabla\delta\varphi : [\boldsymbol{F}\cdot\boldsymbol{S}]\,\mathrm{d}V - \int_{\mathscr{B}_0} \delta\varphi\cdot\boldsymbol{F}^{\varphi}\mathrm{d}V \doteq 0,\end{aligned} \qquad (15)$$

for admisible variations $\delta\Phi$ and $\delta_{\boldsymbol{\varphi}}$.

3.2. Temporal and spatial discretization

To discretize the weak forms (15) in time, we partition the time interval of interest $\mathscr{T}$ into n_{step} discrete subintervals $[t_{\mathrm{n}}, t_{\mathrm{n+1}}]$ of length $\Delta t = t_{\mathrm{n+1}} - t_{\mathrm{n}}$,

$$\mathscr{T} = \bigcup_{\mathrm{n}=1}^{n_{\mathrm{step}}} [t_n, t_{n+1}]. \qquad (16)$$

For the electrical problem, we adopt an implicit Euler backward scheme to determine the electrical potential Φ at the current time point $t_{\mathrm{n+1}}$, and approximate its time derivatives as

$$\dot{\Phi} \approx [\Phi - \Phi_{\mathrm{n}}]/\Delta t. \qquad (17)$$

For the mechanical problem, we adopt a Newmark time discretization to approximate the mechanical acceleration and velocity $\ddot{\varphi}$ and $\dot{\varphi}$ at the current time point $t_{\mathrm{n+1}}$,

$$\begin{aligned}\ddot{\boldsymbol{\varphi}} &\approx 1/[\beta\Delta t^2]\,[\boldsymbol{\varphi} - \boldsymbol{\varphi}_{\mathrm{n}}] - 1/[\beta\Delta t]\,\dot{\boldsymbol{\varphi}}_{\mathrm{n}} - [1 - 2\beta]/[2\beta]\ \ddot{\boldsymbol{\varphi}}_{\mathrm{n}}\\ \dot{\boldsymbol{\varphi}} &\approx \gamma/[\beta\Delta t]\ [\boldsymbol{\varphi} - \boldsymbol{\varphi}_{\mathrm{n}}] + [1 - \gamma/\beta]\,\dot{\boldsymbol{\varphi}}_{\mathrm{n}} + [1 - \gamma/[2\beta]]\,\Delta t\,\ddot{\boldsymbol{\varphi}}_{\mathrm{n}}.\end{aligned} \qquad (18)$$

Typical values for the Newmark parameters are $\beta = 0.25$ and $\gamma = 0.5$, for which Newmark's method is stable and second order accurate for linear problems. To discretize the weak forms of the electrical and mechanical problems (15.1) and (15.2) in space, we partition the domain of interest $\mathscr{B}_0$ into n_{el} discrete subdomains $\mathscr{B}_0^{\mathrm{e}}$,

$$\mathscr{B}_0 = \bigcup_{\mathrm{e}=1}^{n_{el}} \mathscr{B}_0^{\mathrm{e}}, \qquad (19)$$

and adopt a finite element discretization in combination with a classical Bubnov-Galerkin scheme to discretize the test functions $\delta\Phi$ and $\delta\boldsymbol{\varphi}$ and trial functions Φ and $\boldsymbol{\varphi}$ in space within the element domain $\mathscr{B}_0^{\mathrm{e}}$ [18],

$$\begin{array}{ll} \delta\Phi^{\mathrm{e}} = \sum_{i=1}^{n_{el}} N_i\, \delta\Phi_i^{\mathrm{e}} & \delta\varphi^{\mathrm{e}} = \sum_{j=1}^{n_{el}} N_j\, \delta\varphi_j^{\mathrm{e}} \\ \Phi^{\mathrm{e}} = \sum_{k=1}^{n_{el}} N_k\, \Phi_k^{\mathrm{e}} & \varphi^{\mathrm{e}} = \sum_{l=1}^{n_{el}} N_l\, \varphi_l^{\mathrm{e}}. \end{array} \qquad (20)$$

where N represent the standard isoparametric shape functions and $n_{\mathrm{e}1}$ represents the number of nodes per element.

3.3. Residuals and consistent linearization

With the discretizations in time (17,18) and space (20), we can reformulate the weak forms (15) as the discrete algorithmic residuals of the electrical and mechanical problems,

$$\begin{array}{l} \mathrm{R}_I^{\Phi} = \mathop{\mathbf{A}}_{\mathrm{e}=1}^{n_{el}} \int_{\mathscr{B}_0^{\mathrm{e}}} N_i \frac{\Phi - \Phi_{\mathrm{n}}}{\Delta t} + \nabla N_i \cdot \boldsymbol{Q} \quad - N_i F^{\Phi}\, \mathrm{d}V_{\mathrm{e}} \doteq 0 \\ \mathbf{R}_J^{\varphi} = \mathop{\mathbf{A}}_{\mathrm{e}=1}^{n_{el}} \int_{\mathscr{B}_0^{\mathrm{e}}} N_j \rho_0 \ddot{\boldsymbol{\varphi}}\left(\boldsymbol{\varphi}\right) + \nabla N_j \cdot \boldsymbol{F} \cdot \boldsymbol{S} - N_j \boldsymbol{F}^{\varphi}\, \mathrm{d}V_{\mathrm{e}} \doteq \mathbf{0}. \end{array} \qquad (21)$$

The operator **A** symbolizes the assembly of all element residuals at the element nodes i and j to the global residuals at the global nodes I and J. To solve for the unknown nodal electrical potential Φ_I and mechanical deformation $\boldsymbol{\varphi}_J$, we could, for example, adapt an incremental interative Newton-Raphson solution strategy based on the consistent linearization of the governing equations,

$$\begin{array}{l} \mathrm{R}_I^{\Phi} + \sum_K \mathrm{K}_{IK}^{\Phi\Phi} \mathrm{d}\Phi_K + \sum_L \mathbf{K}_{IL}^{\Phi\varphi} \cdot \mathrm{d}\boldsymbol{\varphi}_L \doteq 0 \\ \mathbf{R}_J^{\varphi} + \sum_K \mathbf{K}_{JK}^{\varphi\Phi} \mathrm{d}\Phi_K + \sum_L \mathbf{K}_{JL}^{\varphi\varphi} \cdot \mathrm{d}\boldsymbol{\varphi}_L \doteq \mathbf{0}. \end{array} \qquad (22)$$

The solution of this system of equations (22) with the discrete residuals (21) and the iteration matrices,

$$
\begin{aligned}
\mathrm{K}^{\Phi\Phi}_{IK} &= \overset{n_{el}}{\underset{\mathrm{e}=1}{\mathbf{A}}} \int_{\mathscr{B}^{\mathrm{e}}_0} N_i \left[\tfrac{1}{\Delta t} - \mathrm{d}_{\Phi} F^{\Phi} \right] N_k + \nabla N_i \cdot \boldsymbol{D} \cdot \nabla N_k \quad \mathrm{d}V_{\mathrm{e}} \\
\mathbf{K}^{\Phi\varphi}_{IL} &= \overset{n_{el}}{\underset{\mathrm{e}=1}{\mathbf{A}}} \int_{\mathscr{B}^{\mathrm{e}}_0} \left[N_i \cdot \mathrm{d}_{\boldsymbol{C}} F^{\Phi} + \nabla N_i \cdot \mathrm{d}_{\boldsymbol{C}} \boldsymbol{Q} \right] \cdot \left[\boldsymbol{F}^{\mathrm{t}} \cdot \nabla N_l \right]^{\mathrm{sym}} \quad \mathrm{d}V_{\mathrm{e}} \\
\mathbf{K}^{\varphi\Phi}_{JK} &= \overset{n_{el}}{\underset{\mathrm{e}=1}{\mathbf{A}}} \int_{\mathscr{B}^{\mathrm{e}}_0} \nabla N_j \cdot \mathrm{d}_{\Phi} \boldsymbol{S}^{\mathrm{act}} \cdot N_k \quad \mathrm{d}V_{\mathrm{e}} \\
\mathbf{K}^{\varphi\varphi}_{JL} &= \overset{n_{el}}{\underset{\mathrm{e}=1}{\mathbf{A}}} \int_{\mathscr{B}^{\mathrm{e}}_0} N_j \frac{\rho_0}{\beta \Delta t^2} N_l \boldsymbol{I} + \left[\nabla N_j \cdot \boldsymbol{F} \right]^{\mathrm{sym}} : 2\mathrm{d}_{\boldsymbol{C}} \boldsymbol{S} : \left[\boldsymbol{F}^{\mathrm{t}} \cdot \nabla N_l \right]^{\mathrm{sym}} + \nabla N_j \cdot \boldsymbol{S} \cdot \nabla_l N \, \boldsymbol{I} \ \mathrm{d}V_{\mathrm{e}},
\end{aligned}
\tag{23}
$$

defines the iterative update of the global vector of electrical and mechanical unknowns $\boldsymbol{\Phi}_I \leftarrow \boldsymbol{\Phi}_I + \mathrm{d}\boldsymbol{\Phi}_I$ and $\boldsymbol{\varphi}_J \leftarrow \boldsymbol{\varphi}_J + \mathrm{d}\boldsymbol{\varphi}_J$. Here we have used the symmetric operator $\{\circ\}^{\mathrm{sym}} = \frac{1}{2}\left[\{\circ\} + \{\circ\}^{\mathrm{t}} \right]$ and the total derivative $\mathrm{d}_{\{\bullet\}}\{\circ\} = \mathrm{d}\{\circ\}/\mathrm{d}\{\bullet\}$. It remains to specify the sensitivities of the fluxes $\boldsymbol{Q}$ and $\boldsymbol{S}$ and the source term F^{Φ} with respect to the primary unknowns $\boldsymbol{\Phi}$ and $\boldsymbol{\varphi}$ for the iteration matrices (23.1) to (23.4) [13, 18].

3.4. Internal variables

To integrate the evolution equations of the recovery variable r and the active muscle traction T^{act} in time, we treat both as internal variables and update and store them locally on the integration point level [18, 36]. To solve the nonlinear evolution equation (9) for the recovery variable r, we locally adopt an implicit Euler backward scheme [17, 28],

$$\dot{r} = \left[r - r_k \right] / \Delta t, \tag{24}$$

and introduce the local residual $\mathbf{R}^r$,

$$\mathrm{R}^r = r - r_k - \gamma \Delta t + \frac{\mu_1 r}{\mu_2 + \Phi} \left[r + c\Phi \left[\Phi - b - 1 \right] \right] \Delta t = 0, \tag{25}$$

and its algorithmic linearization $\mathbf{K}^{\tau}$,

$$\mathrm{K}^r = 1 + \frac{\mu_1}{\mu_2 + \Phi} \left[2r - c\Phi \left[\Phi - \beta - 1 \right] \right] \Delta t. \tag{26}$$

We iteratively update the recovery variable as $r \leftarrow \mathrm{r} - \mathbf{R}^r / \mathbf{K}^r$ [34]. To solve the linear evolution equation (13.2) for the active muscle traction T^{act}, we again adopt a finite difference discretization in time together with an implicit Euler backward scheme,

$$\dot{T}^{\mathrm{act}} = \left[T^{\mathrm{act}} - T^{\mathrm{act}}_k \right] / \Delta t, \tag{27}$$

and solve the resulting equation directly to calculate the active muscle traction at the current point in time,

$$T^{\mathrm{act}}=\left[T_k^{\mathrm{act}}+\varepsilon k_T\left[\Phi-\Phi_r\right]\Delta t\right]/\left[1+\varepsilon\Delta t\right]. \qquad (28)$$

Once we have determined the recovery variable r and the active muscle traction T^{act}, we calculate the electrical flux $\boldsymbol{Q}$ from equation (6), the electrical source F_{e}^{Φ} from equation (7), the passive stress $\boldsymbol{S}^{\mathrm{pas}}$ from equation (12), and the active stress $\boldsymbol{S}^{\mathrm{act}}$ from equation (13) to evaluate the electrical and mechanical residuals (21).

3.5. Sensitivities

Last, we calculate the sensitivities $\mathrm{d}_{\boldsymbol{C}}F^{\Phi}$, $\mathrm{d}_{\boldsymbol{C}}\boldsymbol{Q}$, $\mathrm{d}_{\Phi}\boldsymbol{S}^{\mathrm{act}}$, and $\mathrm{d}_{\boldsymbol{C}}\boldsymbol{S}$ for the electrical and mechanical iteration matrices (23),

$$\begin{gathered}
\mathrm{d}_{\boldsymbol{C}}F^{\Phi}=\tfrac{1}{2}\theta G_{\mathrm{S}}[\Phi_{\mathrm{S}}-\Phi]I_4^{-1/2}[\boldsymbol{f}_0\otimes\boldsymbol{f}_0]\\
\mathrm{d}_{\Phi}\boldsymbol{S}^{\mathrm{act}}=\mathrm{d}_{\Phi}T^{\mathrm{act}}I_4^{-1}\boldsymbol{f}_0\otimes\boldsymbol{f}_0\\
\mathrm{d}_{\boldsymbol{C}}\boldsymbol{Q}=[D^{\mathrm{iso}}\tfrac{1}{2}[\boldsymbol{C}^{-1}\overline{\otimes}\,\boldsymbol{C}^{-1}+\boldsymbol{C}^{-1}\underline{\otimes}\,\boldsymbol{C}^{-1}]+D^{\mathrm{ani}}I_4^{-2}[\boldsymbol{f}_0\otimes\boldsymbol{f}_0]\otimes[\boldsymbol{f}_0\otimes\boldsymbol{f}_0]]\cdot\nabla\Phi\\
\mathrm{d}_{\boldsymbol{C}}\boldsymbol{S}=\lambda\boldsymbol{C}^{-1}\otimes\boldsymbol{C}^{-1}-[\tfrac{1}{2}\lambda\ln(I_3)-\mu]\tfrac{1}{2}[\boldsymbol{C}^{-1}\overline{\otimes}\,\boldsymbol{C}^{-1}+\boldsymbol{C}^{-1}\underline{\otimes}\,\boldsymbol{C}^{-1}]+[2\eta\theta-T^{\mathrm{act}}I_4^{-2}][\boldsymbol{f}_0\otimes\boldsymbol{f}_0]\otimes[\boldsymbol{f}_0\otimes\boldsymbol{f}_0],
\end{gathered}$$

(29)

where $\{\circ\overline{\otimes}\bullet\}_{ijkl}=\{\circ\}_{ik}\{\bullet\}_{jl}$ and $\{\circ\underline{\otimes}\bullet\}_{ijkl}=\{\circ\}_{il}\{\bullet\}_{jk}$ Finally, $\mathrm{d}_{\Phi}F^{\Phi}$ and $\mathrm{d}_{\Phi}T^{\mathrm{act}}$ can be found in [34] and [17], respectively.

4. Model problem

In this section we summarize the model problems and their results used to assess the influence of mass and mechano-electrical feedback on the conduction velocity of the electrical wave, and the electromechanical behavior in general. Then, we consider the influence of inertial and mechano-electrical parameters on spiral waves. For each of these studies we considered five cases, plain electrophysiology (EP), electromechanics (EM), electromechanics with mass (EMM), electromechanics with mechano-electrical feedback (EM+MEF), and electromechanics with mass and mechano-electrical feedback (EMM +MEF) as summarized in Table 1.

Table 2 summarizes the electrical, mechanical, and electro-mechanical parameters of these models. To obtain realistic mass-to-stiffness ratios, we calibrated the parameters of the neo-Hookean material model to fit the Holzapfel model [25] in the range of 0 to 15% tensile strain. In these two models, fiber stiffness is only activated when in tension. Given that we are simulating the contraction of cardiac tissue that results mainly in compressive strains in the fiber direction, we consider this neo-Hookean material a good first approximation. We also calibrated the active contraction parameters to obtain strains on the order of 12%, which agree with strains measured *in vivo* [52].

4.1. Conduction velocity study

To study conduction velocity, we consider 5 mm × 5 mm × 10 mm rectangular bar (Figure 1) using time steps of $\Delta t = \{0.005, 0.01, 0.05\}$ ms and mesh sizes of $\Delta x = \{0.1, 0.25, 0.5\}$ mm. We take advantage of the symmetry of the problem by simulating one fourth of the cross section. As mechanical boundary conditions, we fix the plane $x = 0$ mm in the x direction, the plane $y = 0$ mm in the y direction, and the plane $z = 0$ mm in the z direction. To initiate a planar wave front, we apply a surface flux of 30 mV/(ms mm^2) in the plane $x = 0$ mm at time t_0. We compute the conduction velocity in the reference configuration with the activation times at $x = 2.5$ mm and $x = 7.5$ mm. We define the activation time as the moment when the action potential reaches 0mV. To better approximate the activation times, we linearly interpolate between two discrete time points.

Figure 2 and Tables 3 and 4 summarize the results from the conduction velocity study. As presented in Figure 2, refining the time discretization decreases the conduction velocity and refining the mesh size increases the conduction velocity. The conduction velocities range between 0.374 m/s for $\Delta x = 0.5$ mm, $\Delta t = 0.005$ ms to 0.431 m/s for $\Delta x = 0.1$ mm, $\Delta t = 0.05$ ms. The variations in conduction velocity, however, can be considered small, falling below 5% for all models when compared to the smallest time step and mesh size for each model. We observe that the biggest impact on conduction velocity is caused by including mechano-electrical feedback in the model (EM+MEF). The addition of this mechanism leads to an increase of 6% in conduction velocity when compared to the purely electrophysiological model (EP). The inclusion of inertia in the electromechanical model (EMM+MEF) further exacerbates the effect of mechano-electrical feedback, increasing the conduction velocity by 8% when compared to the EP case. We explain this difference by the additional displacements caused by the inertial effect, which are translated into additional current via the mechano-electrical feedback. This observation is further supported by the small difference in conduction velocity between the electromechanics model with mass (EMM) and without mass (EM). In this case, the inertial displacements do not generate additional currents, and the difference in conduction velocity can be attributed to the coupling between the electrical flux and the deformation. With this in mind, we can quantify the cumulative contributions to the increment in conduction velocity as a 2% caused by electrical flux coupling, 4% caused by the mechano-electrical feedback and a final 2% caused by the inertial effect.

Figure 3 illustrates the sensitivity of the conduction velocity to the mechano-electrical feedback. We systematically vary the parameter G_s from 0 to 25 using the same geometry with $\Delta x = 0.5$ mm and $\Delta t = 0.05$ ms. Figure 3 shows that the conduction velocity increases with G_s for the cases with and without mass. However, this effect is more prominent in the case with mass. The differences in conduction velocity between the case with mass and without mass increases from 0.2% for $G_s = 0$ to 2.6% for $G_s = 25$.

Figure 4 highlights the response of the different models for a segment of the cardiac wall excited in three regions. The simulation covers the isovolumetric contraction phase during the cardiac cycle. Figure 4, left, illustrates the 20 mm ×20 mm × 10 mm block to represent a region of the cardiac wall, which we excite in three arbitrary elements on the endocardial surface with a body flux of 300 mV/(ms · mm^3). This boundary condition mimics the activation by the Purkinje network, which is only connected at discrete points to the myocardial tissue [49]. We fix all faces of the block in their normal direction except the epicardial surface and we set $\Delta x = 0.5$ mm and $\Delta t = 0.05$ ms. As an indicator of conduction velocity in this irregular activation pattern, we use the time to completely activate the block. The results show that the differences in conduction velocity now can be mainly attributed to the mechano-electrical feedback. The electromechanics coupling (EM) and inertia (EMM) have little impact on the total activation time, with differences lower that 0.3% when compared to the plain electrophysiology case (EP). The addition of mechano-electrical feedback (EM+MEF, EMM+MEF) leads to a reduction of more than 8% in the total activation time when compared to the other cases (EP, EM, EMM). There is virtually no difference, <0.1%, in the total activation time between the mechano-electrical feedback cases without mass (EM+MEF) and with mass (EMM+MEF), which suggests that inertia does not play a significant role in this simulation.

4.2. Spiral wave trajectory

Figure 5 illustrates a slab of tissue with dimension 50 mm × 50 mm × 5 mm in which we study the effect of mass on spiral waves. We set the element size to 0.5 mm and an adaptive time step limited to 0.5 ms. We connect all the boundary of the tissue with springs pointing in the normal direction of the surface and set the stiffness of these springs to $4.5 \cdot 10^{-8}$ N/mm to ensure convergence while leaving the tissue fairly unconstrained. To create the spiral wave, we adopt an S1–S2 protocol. We first apply a stimulus S1 of 12mV/(ms mm^2) for 2ms in the plane $x = 0$mm to create a planar wave front. After 290ms, we apply a stimulus S2 of 15mV/(ms mm^3) in the quadrant $\{x < 25, y < 25\}$ mm for 5ms. Finally, we simulate the spiral wave for 1000 ms. As a post-processing step, we track the spiral tip through the entire timespan of the simulation. We calculate the position of the spiral tip as the intersection of two isopotential lines at $\Phi = -30$ mV of two consecutive time points at the $z = 0$ plane in the reference configuration [14]. For each rotation, we compute the spiral center position as the mean of all points on the trajectory. We calculate the spiral center velocity by taking the norm over the difference of two consecutive center positions and dividing it by the rotation time.

Figure 6 shows the transmembrane potential and fiber stretch fields for all cases during the planar wave propagation stage and by the end of the simulation, when spirals are present. At time 50 ms, compressive stretches are produced in the activated regions, where the action potential is high. We observe that the inclusion of mass alters the stretch distribution in the upper and lower boundaries. The differences are accentuated when the spiral wave develops. In the cases with mass, considerable regions of the tissue experience tensile stretch not present in the cases where mass is neglected.

Figure 7 illustrates a consequence of mechano-electrical feedback, where wave fronts are generated in secondary locations when the combination of mass and mechano-electrical feedback is included. The high tensile stretch observed in the upper boundary of the case with mass and mechano-electrical feedback is followed by the activation of this region 10 ms later. This wavefront later collides with the existing spiral at time 144 ms, while another wavefront appears in the lower boundary. In the absence of inertial effects, the tensile stretches generated solely by the active contraction are lower in magnitude and are not able to generate additional wave fronts.

Figure 8 shows the emergent spiral wave dynamics by means of the spiral wave center trajectories for all models. All trajectories show different directions and lengths, displaying an important model dependency of this variable. The spiral waves in the electrophysiology (EP) and mass and mechano-electrical feedback (EMM+MEF) cases drift to the left while they drift to the right for the remaining three cases (EM, EM+MEF, EMM). We also observe two trends: first, mechano-electrical feedback tends to decrease the trajectory length with or without mass. Figure 6 shows that in the vicinity of the spiral tip, there are regions of tensile fiber stretch. The mechano-electrical current generated in this region could stabilize the spiral wave. Second, we see that the cases when mass was included have longer trajectories for the same amount of time. When we compare the spiral center speed in Figure 9 we observe that, for most rotations, the speed is higher when mass is considered. Towards the end, the speed increases for the cases with mass, suggesting that the spiral would continue drifting. For the cases without mass, we see the opposite: the spiral center speed tends to zero, suggesting that spiral would continue to be stable.

5. Discussion

In this work, we systematically studied the role of inertia and mechano-electrical feedback in cardiac electromechanics models. As a first step, we considered simple geometries to accurately assess the impact on electrophysiological and mechanical metrics. However, we believe our results translate directly into more realistic models, despite the inherent geometrical complexities [30] or boundary conditions [3]. In these sophisticated models, we expect to see a major influence in the electrical propagation of the mechano-electrical feedback and a minor influence of the inertia term in both the electrical and mechanical behavior. Nonetheless, we plan to incorporate our findings into a four-chamber, high resolution heart simulator [4] and explore the influence of inertia and mechano-electrical currents on clinically relevant variables such as electrocardiograms [34, 35, 26, 49] and pressure-volume loops [16]. We also plan to include a more sophisticated material model and study the effects of viscosity [22, 44]. Additionally, we would like to include the effect of stretch and velocity in the active contraction model [21, 47, 50, 38], to simulate relevant macroscopic characteristics of the heart, such as the Frank-Starling effect. Our modular approach allows us to easily incorporate these changes in our model.

In this study, we explored the differences between including mass and/or including mechano-electrical feedback using our fully coupled finite element electromechanical formulation. Our major finding is that the additional deformation caused by inertia alters the electrical wave dynamics when mechano-electrical currents are present. We observed that the inclusion of mass and mechano-electrical feedback lead to highest increase in conduction velocity. However, the inclusion of mass solely did not alter the conduction velocity compared to the plain electromechanics case. Taken together, this suggests that inertia is generating tensile stretches that initiate mechano-electrical currents, which add to the wave propagation. This observation was further confirmed by our spiral wave study. Figure 6 shows higher tensile stretches for both cases with mass. Moreover, Figure 7 shows the extreme case when the tensile stretches are large enough to create mechano-electrical currents that lead to an additional wave front. We also observed that the inclusion of mass leads to a larger and faster spiral drift, which is associated with polyformic ventricular tachycardia, a precursor of ventricular fibrillation [20, 54]. Recent studies have shown that knowing the precise position of the spiral wave center is critical when attempting to terminate atrial fibrillation through localized ablation [46].

From a computational point of view, our model showed little sensitivity to the spatial and temporal discretization. In the conduction velocity study, the maximum difference was less than 5% for all cases, which is considerable smaller than the 50% of variation that other formulations exhibit for the same range of time increments and mesh sizes [42]. Our model is able to handle the anisotropic architecture of cardiac tissue at the electrical and mechanical levels, with complex wave spiral waves and heterogeneous deformations induced by inertial effects. Ultimately, our model will help the research community to better understand the complex interactions that govern the heart’s function.

Acknowledgments

This model was developed within the Living Heart project, and we acknowledge the technical support Brian Baillargeon and Nuno Rebelo at Dassault Systèmes Simulia Corporation. This study was supported by the Stanford Cardiovascular Institute seed fund, by Stanford School of Engineering Fellowship, and by the Becas Chile-Fulbright Fellowship to Francisco Sahli Costabal, by Conicyt Chile through “Becas de estadía corta” to Felipe Concha, by Conicyt Chile through Fondecyt Grant 11121224 to Daniel Hurtado, and by the National Institutes of Health Grant U01-HL119578 to Francisco Sahli Costabal and Ellen Kuhl.

A. Appendix: Abaqus Implementation

In this Appendix, we illustrate the specific implementation of the electromechanics problem into the finite element software package Abaqus/Standard [1]. We took advantage of the existing coupled thermal-displacement procedure in Abaqus. By setting the density and the specific heat to unity, we recover the balance equations (4). However, this procedure neglects the inertia term in equation (4.2). To analyze the effect of mass, we superimposed a user element to the standard element as is explained in (A.3). In the following, we explain the different subroutines used to create the electromechanical model.

A.1. User material - UMAT

In this subroutine, we calculate the passive stress, the active stress, and the mechanical transmembrane current with their corresponding sensitivities. We use the left Cauchy-Green deformation tensor,

$$\boldsymbol{b}=\boldsymbol{F}\cdot\boldsymbol{F}^{t}. \quad (30)$$

Abaqus/Standard uses the Cauchy stresses, $\boldsymbol{\sigma}^{\text{pas}}$ and $\boldsymbol{\sigma}^{\text{act}}$, which follow from the push forward, $\boldsymbol{\sigma} = \boldsymbol{F} \cdot \boldsymbol{S} \cdot \boldsymbol{F}^{\text{t}}/\text{J}$, of the Piola-Kirchhoff stresses, S^{pas} and S^{act}, in equations (12) and (13),

$$\begin{gathered}\boldsymbol{\sigma}^{\text{pas}}=\left[\left[\tfrac{1}{2}\lambda\ln\left(I_3\right)-\mu\right]\boldsymbol{I}+\mu\boldsymbol{b}+2\theta\eta\left[I_4-1\right]\boldsymbol{f}\otimes\boldsymbol{f}\right]/J\\ \boldsymbol{\sigma}^{\text{act}}=T^{\text{act}}I_4^{-1}\boldsymbol{f}\otimes\boldsymbol{f}/J.\end{gathered} \quad (31)$$

For the stress sensitivity, Abaqus uses the Jauman stress rate of the Kirchhoff stress divided by the Jacobian, $\mathbb{C}^{\text{abaqus}}=\mathbb{C}+\mathbb{C}'$ [23], where $\mathbb{C}$ is the Eulerian elasticity tensor, which follows from the push forward, $\mathbb{C}=[\boldsymbol{F}\overline{\otimes}\boldsymbol{F}]:\mathbb{C}:\left[\boldsymbol{F}^{\text{t}}\underline{\otimes}\boldsymbol{F}^{\text{t}}\right]/J$ of the Lagrangian elasticity tensor, $\mathbb{C}=2\text{d}\boldsymbol{S}/\text{d}\boldsymbol{C}$, from equation (29.4),

$$\mathbb{C}=[\lambda\boldsymbol{I}\otimes\boldsymbol{I}-[\frac{1}{2}\lambda\ln\left(I_3\right)-\mu][\boldsymbol{I}\overline{\otimes}\boldsymbol{I}+\boldsymbol{I}\underline{\otimes}\boldsymbol{I}]+[4\eta\theta-2T^{\text{act}}I_4^{-2}][\boldsymbol{f}\otimes\boldsymbol{f}]\otimes[\boldsymbol{f}\otimes\boldsymbol{f}]]/J, \quad (32)$$

and ¢′ is a correction for the Jauman rate

$$\mathbb{C}'=\frac{1}{2}[\boldsymbol{I}\overline{\otimes}\boldsymbol{\sigma}+\boldsymbol{I}\underline{\otimes}\boldsymbol{\sigma}+\boldsymbol{\sigma}\overline{\otimes}\boldsymbol{I}+\boldsymbol{\sigma}\underline{\otimes}\boldsymbol{I}]. \quad (33)$$

A crucial step in this subroutine is the computation of the spatial fiber vector f. When using local orientations, Abaqus rotates the local coordinate system using the rotation matrix $\boldsymbol{R}$ of the polar decomposition of the deformation gradient, $\boldsymbol{F} = \boldsymbol{v} \cdot \boldsymbol{R}$, where $\boldsymbol{v}$ is the left stretch tensor. We now seek to compute $\mathbf{f}'$, which is the spatial fiber vector in the rotated coordinate system. We define $\hat{\boldsymbol{f}}_0=\boldsymbol{R}^t\cdot\boldsymbol{f}_0$ as the fiber vector rotated only by rigid body motion. These two vectors have the same components, but in different coordinate systems, such that $\hat{f}_{0i}'=f_{0i}$ We start from the definition of $\boldsymbol{f} = \boldsymbol{F} \cdot \boldsymbol{f}_0$, or equivalently, $\boldsymbol{R}\cdot\boldsymbol{f}'=\boldsymbol{F}\cdot\boldsymbol{R}\cdot\boldsymbol{f}_0'$ Premultiplying this equation with $\boldsymbol{R}^{-1} = \boldsymbol{R}^{\text{t}}$ yields,

$\boldsymbol{f}'=\boldsymbol{R}^{\text{t}}\cdot\boldsymbol{F}\cdot\boldsymbol{R}\cdot\boldsymbol{f}_0'=\boldsymbol{F}'\cdot\boldsymbol{f}_0'=\boldsymbol{F}'\cdot\boldsymbol{R}^t\cdot\hat{\boldsymbol{f}}_0'=v'\cdot\boldsymbol{R}\cdot\boldsymbol{R}^t\cdot\hat{\boldsymbol{f}}_0'=v'\cdot\hat{\boldsymbol{f}}_0'$ We can now proceed to calculate the spatial fiber vector in the rotated coordinate system using the polar decomposition of the deformation gradient, $\boldsymbol{F}' = \boldsymbol{v}' \cdot \boldsymbol{R}$. Finally, we can directly implement the mechano-electrical source term in the form of equation (10),

$$F_{\text{m}}^{\Phi}=\theta G_{\text{s}}\left[\lambda-1\right]\left[\Phi_{\text{s}}-\Phi\right], \quad (34)$$

and calculate the push forward, $\text{d}_{\boldsymbol{g}}F_{\text{m}}^{\Phi}=\text{d}_{\boldsymbol{b}}F_{\text{m}}^{\Phi}\cdot\boldsymbol{b}=\boldsymbol{F}\cdot\text{d}_{\boldsymbol{C}}F_{\text{m}}^{\Phi}\cdot\boldsymbol{F}^{\text{t}}/J$, of its sensitivity, $\text{d}_{\boldsymbol{C}}F^{\Phi}=\frac{1}{2}\theta G_{\text{s}}\left[\Phi_{\text{s}}-\Phi\right]\lambda^{-1}\left[\boldsymbol{f}_0\otimes\boldsymbol{f}_0\right]$, from equation (29.1),

$$\mathrm{d}_{\boldsymbol{g}} F_{\mathrm{m}}^{\Phi} = \mathrm{d}_{\boldsymbol{b}} F_{\mathrm{m}}^{\Phi} \cdot \boldsymbol{b} = \frac{1}{2} \theta G_{\mathrm{S}} \left[\Phi_{\mathrm{S}} - \Phi \right] \lambda^{-1} \, \boldsymbol{f} \otimes \boldsymbol{f} / J. \tag{35}$$

A.2. Nonlinear source term - HETVAL

This subroutine is designed to define thermal body flux, which can depend on internal variables [1]. In our formulation, we can use this body flux to represent the transmembrane current F_{e}^{Φ}. In this subroutine, we evaluate equations (24) to (26) with a local Newton-Raphson solver to update the internal variable r and the magnitude of the current F_{e}^{Φ} (using equation (8).

A.3. User element - UEL

To include the effects of inertia, we superimpose user elements that share their nodes with the coupled thermaldisplacement elements of Abaqus/Standard. To compute the accelerations and velocities, we adopt Newmark's method (18) and store these quantities as internal variables in the user element. To superpose these effects to the quasi-static solution, we add an inertia term to the mechanical residual,

$$\mathbf{R}_{J}^{\varphi} \overset{n_{el}}{\underset{\mathrm{e}=1}{\mathbf{A}}} \int_{\mathscr{B}_0^{\mathrm{e}}} N_j \rho_0 \ddot{\boldsymbol{\varphi}} \, \mathrm{d}V_{\mathrm{e}}, \tag{36}$$

and the corresponding linearization term, the consistent mass matrix, to the mechanical tangent operator,

$$\mathbf{K}_{JL}^{\varphi\varphi} = \overset{n_{el}}{\underset{\mathrm{e}=1}{\mathbf{A}}} \int_{\mathscr{B}_0^{\mathrm{e}}} N_j \frac{\rho_0}{\beta \Delta t^2} N_l \boldsymbol{I} \, \mathrm{d}V_{\mathrm{e}}. \tag{37}$$

We specify the tissue density ρ_0 as an element property.

References

1. Abaqus 6.14. Abaqus Analysis User's Guide. SIMULIA, Dassault Systèmes; 2014.
2. Aliev RR, Panfilov AV. A simple two-variable model of cardiac excitation. Chaos, Solitons and Fractals. 1996; 7(3):293–301.
3. Asner L, Hadjicharalambous M, Chabiniok R, Peressutti D, Sammut E, Wong J, Carr-White G, Razavi R, Smith N, Lee J, Nordsletten D. Patient-specific modeling for left ventricular mechanics using data-driven boundary energies. Comp Meth Appl Mech Eng. 2017; doi: 10.1016/j.cma.2016.08.002
4. Baillargeon B, Rebelo N, Fox D, Taylor R, Kuhl E. The Living Heart Project: A robust and integrative simulator for human heart function. European Journal of Mechanics A/Solids. 2014; 48:38–47. [PubMed: 25267880]
5. Berberoglu E, Onur Solmaz H, Göktepe S. Computational modeling of coupled cardiac electromechanics incorporating cardiac dysfunctions. European Journal of Mechanics, A/Solids. 2014; 48(1):60–73.

6. Bonet, J., Wood, R. Nonlinear continuum mechanics for finite element analysis. 2nd. Cambridge University Press; Cambridge: 2008.
7. Cave DM, Gazmuri RJ, Otto CW, Nadkarni VM, Cheng A, Brooks SC, Daya M, Sutton RM, Branson R, Hazinski MF. Part 7: CPR techniques and devices: 2010 American Heart Association Guidelines for Cardiopulmonary Resuscitation and Emergency Cardiovascular Care. 2010
8. Chabiniok R, Wang V, Hadjicharalambous M, Asner L, Lee J, Sermesant M, Kuhl E, Young A, Moireau P, Nash M, Chapelle D, Nordsletten D. Multiphysics and multiscale modeling, data-model fusion and integration of organ physiology in the clinic: ventricular cardiac mechanics. Interface Focus. 2016; 6:20150083. [PubMed: 27051509]
9. Chapelle D, Fernández MA, Gerbeau JF, Moireau P, Sainte-Marie J, Zemzemi N. Numerical simulation of the electromechanical activity of the heart. Lecture Notes in Computer Science. 2009; 5528:357–365.
10. Cherubini C, Filippi S, Nardinocchi P, Teresi L. An electromechanical model of cardiac tissue: Constitutive issues and electrophysiological effects. Progress in Biophysics and Molecular Biology. 2008; 97(2–3):562–573. [PubMed: 18353430]
11. Clayton R, Bernus O, Cherry E, Dierckx H, Fenton F, Mirabella L, Panfilov A, Sachse F, Seemann G, Zhang H. Models of cardiac tissue electrophysiology: Progress, challenges and open questions. Progress in Biophysics and Molecular Biology. 2011; 104(1–3):22–48. [PubMed: 20553746]
12. Dal H, Göktepe S, Kaliske M, Kuhl E. A fully implicit finite element method for bidomain models of cardiac electrophysiology. Computer Methods in Biomechanics and Biomedical Engineering. 2012; 15(6):645–656. [PubMed: 21491253]
13. Dal H, Göktepe S, Kaliske M, Kuhl E. A fully implicit finite element method for bidomain models of cardiac electromechanics. Computer Methods in Applied Mechanics and Engineering. 2013; 253:323–336. [PubMed: 23175588]
14. Fenton F, Karma A. Vortex dynamics in three-dimensional continuous myocardium with fiber rotation: Filament instability and fibrillation. Chaos (Woodbury, NY). 1998; 8(1):20–47.
15. FitzHugh R. Impulses and physiological states in theoretical models of nerve membrane. Biophysical Journal. 1961; 1(6):445–466. [PubMed: 19431309]
16. Genet M, Lee LC, Baillargeon B, Guccione JM, Kuhl E. Modeling pathologies of diastolic and systolic heart failure. Annals of Biomedical Engineering. 2016; 44(1):112–127. [PubMed: 26043672]
17. Göktepe S, Kuhl E. Computational modeling of cardiac electrophysiology: A novel finite element approach. International Journal for Numerical Methods in Engineering. 2009; 79(2):156–178.
18. Göktepe S, Kuhl E. Electromechanics of the heart: A unified approach to the strongly coupled excitation-contraction problem. Computational Mechanics. 2010; 45:227–243.
19. Göktepe S, Menzel A, Kuhl E. The generalized Hill model: A kinematic approach towards active muscle contraction. J Mech Phys Solids. 2014; 72:20–39. [PubMed: 25221354]
20. Gray RA, Jalife J, Panfilov A, Baxter WT, Cabo C, Davidenko JM, Pertsov AM. Nonstationary vortexlike reentrant activity as a mechanism of polymorphic ventricular tachycardia in the isolated rabbit heart. Circulation. 1995; 91(9):2454–2469. [PubMed: 7729033]
21. Guccione JM, Waldman LK, McCulloch AD. Mechanics of active contraction in cardiac muscle: Part II-Cylindrical models of the systolic left ventricle. Journal of Biomechanical Engineering. 1993; 115(1):82–90. [PubMed: 8445902]
22. Güoltekin O, Sommer G, Holzapfel GA. An orthotropic viscoelastic model for the passive myocardium: continuum basis and numerical treatment. Computer Methods in Biomechanics and Biomedical Engineering. 2016; 19:1647–1664. [PubMed: 27146848]
23. Holland MA, Miller KE, Kuhl E. Emerging brain morphologies from axonal elongation. Annals of Biomedical Engineering. 2015; 43(7):1640–1653. [PubMed: 25824370]
24. Holzapfel G. Nonlinear Solid Mechanics: A Continuum Approach for Engineering. 2000
25. Holzapfel GA, Ogden RW. Constitutive modelling of passive myocardium: a structurally based framework for material characterization. Philosophical Transactions. Series A, Mathematical, Physical, and Engineering Sciences. 2009; 367:3445–3475.

26. Hurtado D, Kuhl E. Computational modelling of electrocardiograms: repolarisation and T-wave polarity in the human heart. Computer Methods in Biomechanics and Biomedical Engineering. 2014; 17(9):986–996. [PubMed: 23113842]
27. Hurtado DE, Castro S, Gizzi A. Computational modeling of non-linear diffusion in cardiac electrophysiology: A novel porous-medium approach. Computer Methods in Applied Mechanics and Engineering. 2016; 300:70–83.
28. Hurtado DE, Henao D. Gradient flows and variational principles for cardiac electrophysiology: toward efficient and robust numerical simulations of the electrical activity of the heart. Computer Methods in Applied Mechanics and Engineering. 2014; 273:238–254.
29. Jie X, Gurev V, Trayanova N. Mechanisms of mechanically induced spontaneous arrhythmias in acute regional ischemia. Circulation Research. 2010; 106(1):185–192. [PubMed: 19893011]
30. Kaminsky D, Hsu M, Yu Y, Evans J, Sacks M, Hughes T. Immersogeometric cardiovascular fluid-structure interaction analysis with divergence-conforming B-splines. Comp Meth Appl Mech Eng. 2017; doi: 10.1016/j.cma.2016.07.028
31. Keldermann RH, Nash MP, Gelderblom H, Wang VY, Panfilov AV. Electromechanical wavebreak in a model of the human left ventricle. American journal of physiology Heart and circulatory physiology. Jul; 2010 299(1):H134–43. [PubMed: 20400690]
32. Keldermann RH, Nash MP, Panfilov AV. Pacemakers in a reaction-diffusion mechanics system. Journal of Statistical Physics. 2007; 128(1–2):375–392.
33. Kohl P, Nesbitt AD, Cooper PJ, Lei M. Sudden cardiac death by Commotio cordis: Role of mechano-electric feedback. 2001
34. Kotikanyadanam M, Göktepe S, Kuhl E. Computational modeling of electrocardiograms: A finite element approach toward cardiac excitation. International Journal for Numerical Methods in Biomedical Engineering. 2010; 26(5):524–533.
35. Krishnamoorthi S, Perotti L, Bergstrom N, Ajijola O, Frid A, Ponnaluri A, Weiss J, Qu Z, Klug W, Ennis D, Garfinkel A. A viscoelastic constitutive modeling framework with variational updates for the myocardium. PLoS ONE. 2014; 9:e114494. [PubMed: 25493967]
36. Krishnamoorthi S, Sarkar M, Klug WS. Numerical quadrature and operator splitting in finite element methods for cardiac electrophysiology. International Journal for Numerical Methods in Biomedical Engineering. 2013; 29(11):1243–1266. [PubMed: 23873868]
37. Lee L, Genet M, Dang A, Ge L, Guccione J, Ratcliffe M. Applications of computational modeling in cardiac surgery. J Cardiac Surg. 2014; 29:293–302.
38. Lumens J, Delhaas T, Kirn B, Arts T. Three-wall segment (TriSeg) model describing mechanics and hemodynamics of ventricular interaction. Annals of Biomedical Engineering. 2009; 37(11): 2234–2255. [PubMed: 19718527]
39. Mozaffarian D, Benjamin EJ, Go AS, Arnett DK, Blaha MJ, Cushman M, de Ferranti S, Despres JP, Fullerton HJ, Howard VJ, et al. Heart disease and stroke statistics-2015 update: a report from the american heart association. Circulation. 2015; 131(4):e29. [PubMed: 25520374]
40. Nagumo J, Arimoto S, Yoshizawa S. An active pulse transmission line simulating nerve axon. Proceedings of the IRE. 1962; 50(10):2061–2070.
41. Nash MP, Panfilov AV. Electromechanical model of excitable tissue to study reentrant cardiac arrhythmias. Progress in Biophysics and Molecular Biology. 2004; 85(2–3):501–522. [PubMed: 15142759]
42. Niederer SA, Kerfoot E, Benson AP, Bernabeu MO, Bernus O, Bradley C, Cherry EM, Clayton R, Fenton FH, Garny A, Heidenreich E, Land S, Maleckar M, Pathmanathan P, Plank G, Rodríguez JF, Roy I, Sachse FB, Seemann G, Skavhaug O, Smith NP. Verification of cardiac tissue electrophysiology simulators using an N-version benchmark. Philosophical ransactions. Series A, Mathematical, Physical, and Engineering Sciences. 2011; 369:4331–4351.
43. Panfilov AV, Keldermann RH, Nash MP. Self-organized pacemakers in a coupled reaction-diffusion-mechanics system. Physical Review Letters. 2005; 95(25):5–8.
44. Ponnaluri A, Perotti L, Ennis D, Klug W. A viscoelastic constitutive modeling framework with variational updates for the myocardium. Comp Meth Appl Mech Eng. 2017; 314:85–101.
45. Pool R. Heart like a wheel. Science. 1990; 247(4948):1294–1295. [PubMed: 2315697]

46. Rappel W, Zaman J, Narayan S. Mechanisms for the termination of atrial fibrillation by localized ablation: Computational and clinical studies. Circ Arrhtythm Electrophysiol. 2015; 8:1325–1333.
47. Rice JJ, Wang F, Bers DM, de Tombe PP. Approximate model of cooperative activation and crossbridge cycling in cardiac muscle using ordinary differential equations. Biophysical Journal. 2008; 95(5):2368–2390. [PubMed: 18234826]
48. Rogers JM, McCulloch AD. A collocation-Galerkin finite element model of cardiac action potential propagation. IEEE Transactions on Biomedical Engineering. 1994; 41(8):743–757. [PubMed: 7927397]
49. Sahli Costabal F, Hurtado DE, Kuhl E. Generating Purkinje networks in the human heart. Journal of Biomechanics. 2015; 49:2455–2465. [PubMed: 26748729]
50. Sainte-Marie J, Chapelle D, Cimrman R, Sorine M. Modeling and estimation of the cardiac electromechanical activity. Computers and Structures. 2006; 84(28):1743–1759.
51. Sermesant M, Delingette H, Ayache N. An electromechanical model of the heart for image analysis and simulation. IEEE Transactions on Medical Imaging. 2006; 25(5):612–625. [PubMed: 16689265]
52. Tsamis A, Bothe W, Kvitting JPE, Swanson JC, Miller DC, Kuhl E. Active contraction of cardiac muscle: in vivo characterization of mechanical activation sequences in the beating heart. Journal of the mechanical behavior of biomedical materials. 2011; 4(7):1167–1176. [PubMed: 21783125]
53. Usyk TP, LeGrice IJ, McCulloch AD. Computational model of three-dimensional cardiac electromechanics. Computing and Visualization in Science. 2002; 4(4):249–257.
54. Weise LD, Panfilov AV. A discrete electromechanical model for human cardiac tissue: Effects of stretch-activated currents and stretch conditions on restitution properties and spiral wave dynamics. PLoS ONE. 2013; 8(3):0059317.

Highlights

- ► Modeling cardiac electromechanics is critical to predict mechanisms of cardiac dysfunction
- ► We study two commonly neglected effects of cardiac electromechanics: mechano-electrical feedback and inertia
- ► We show that conduction velocities and spiral wave dynamics are sensitive to these effects
- ► Mechano-electrical feedback and inertia may initiate secondary waves and shift trajectories
- ► Correctly identifying the trajectories of spiral wave centers can improve ablation therapies

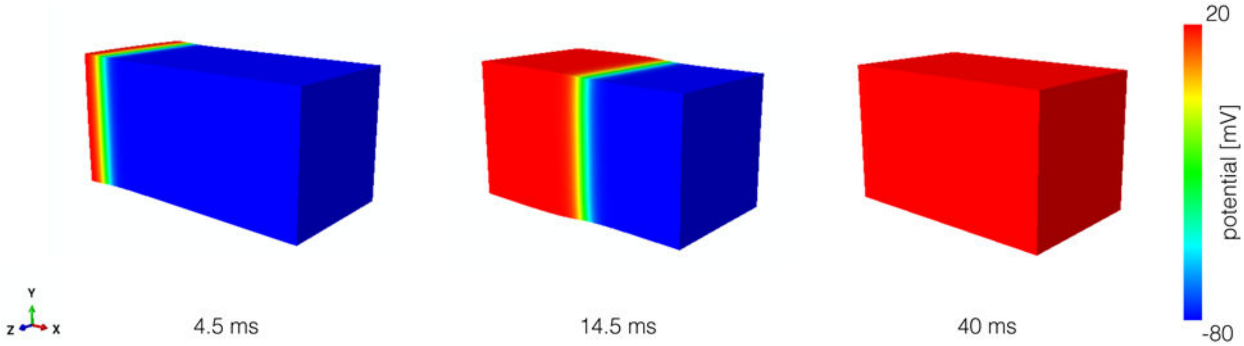

Figure 1.

Simulation protocol to study conduction velocity. We apply a stimulus at the $x = 0$ mm plane to generate a planar wavefront. Then, we allow the entire bar to activate in 40 ms.

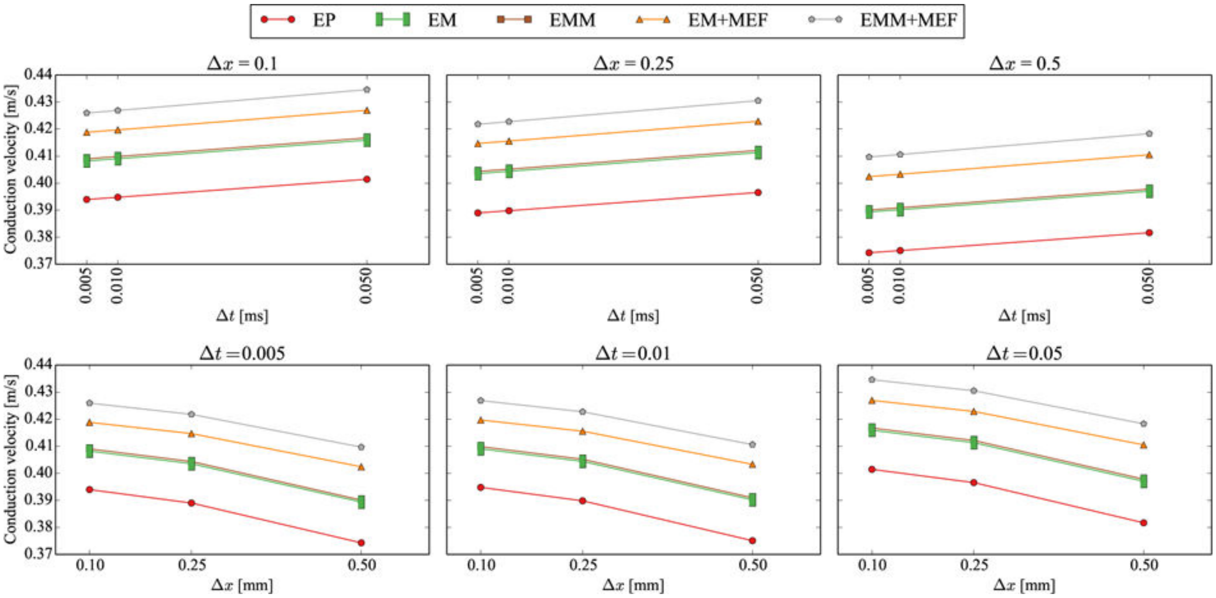

Figure 2.

Results of the conduction velocity study. In the upper row, we observe that refining the time increment reduces the conduction velocity for a given mesh size. In the lower row, we see that refining the mesh size produces the opposite effect, increasing the conduction velocity.

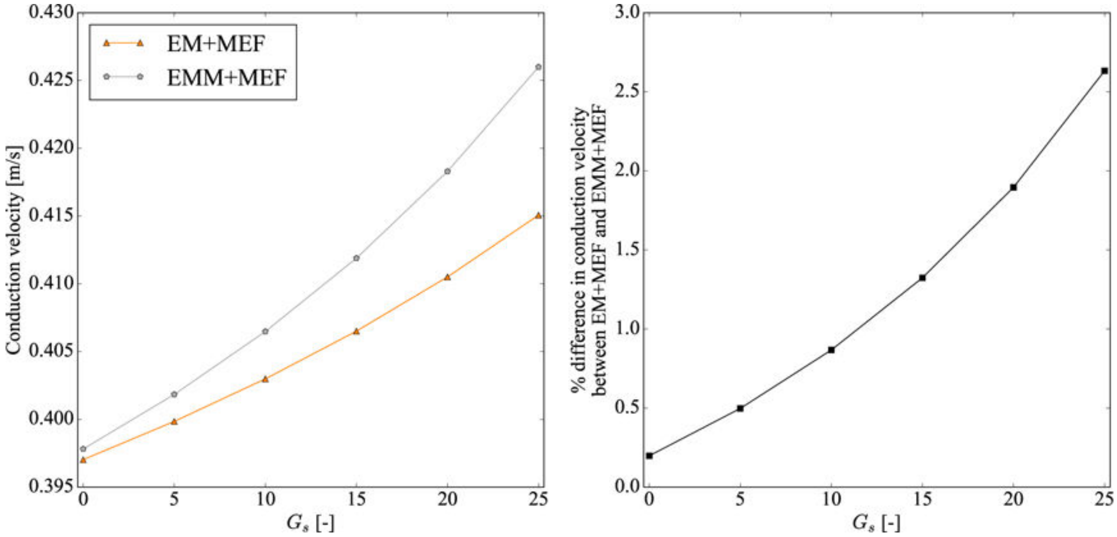

Figure 3.

Effect of mechano-electrical feedback parameter G_s on conduction velocity. The left panel shows the conduction velocity values for the cases without mass (EM+MEF) and with mass (EMM+MEF). The right panel shows the percentual differences in conduction velocity between both cases, using the case without mass (EM+MEF) as reference.

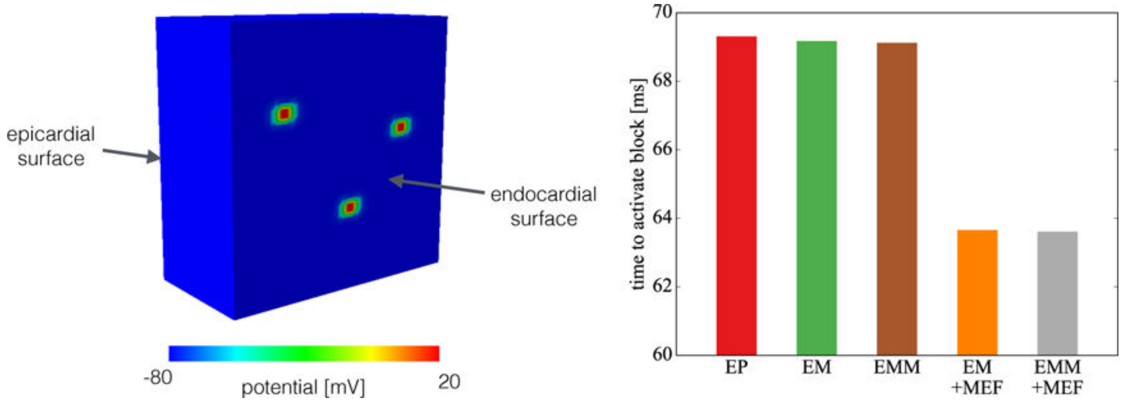

Figure 4.

Simplified model of *in vivo* conditions. We simulate the isovolumetric contraction phase of the cardiac cycle by fixing all faces of the block except the epicardial surface. We activate three arbitrary elements to simulate the Purkinje network interaction with the tissue. We observe the total time to activate the entire block is mainly dependent on the presence of mechano-electrical feedback, which increases the conduction velocity.

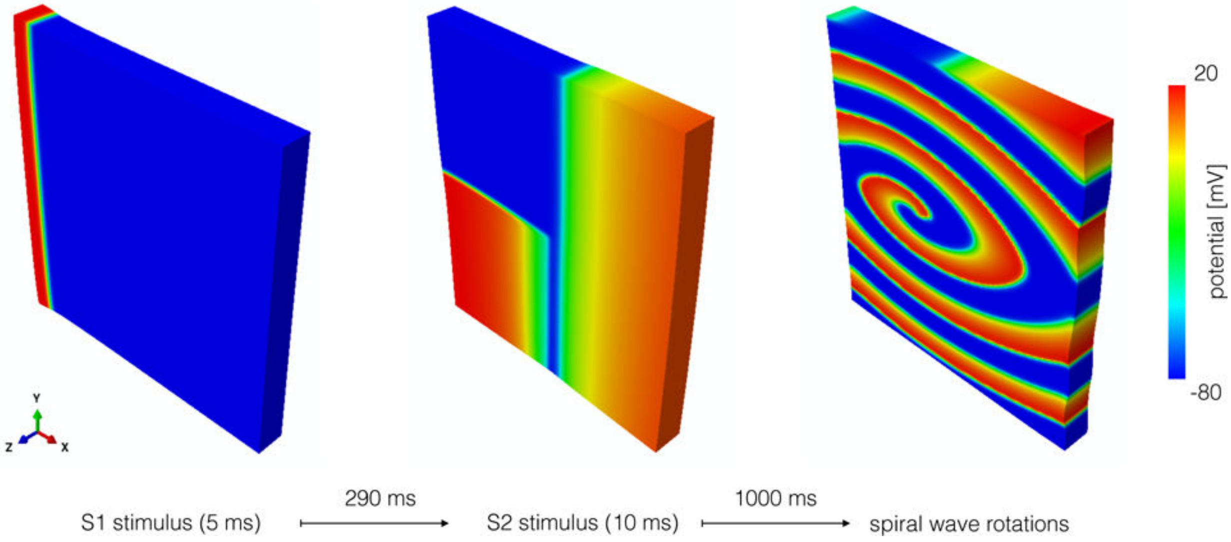

Figure 5.

Simulation protocol to study spiral waves. First, a stimulus S1 is applied in the $x = 0$ plane to generate a planar wavefront. Later, a stimulus S2 is applied in the tail of the wave to trigger the formation of a spiral wave.

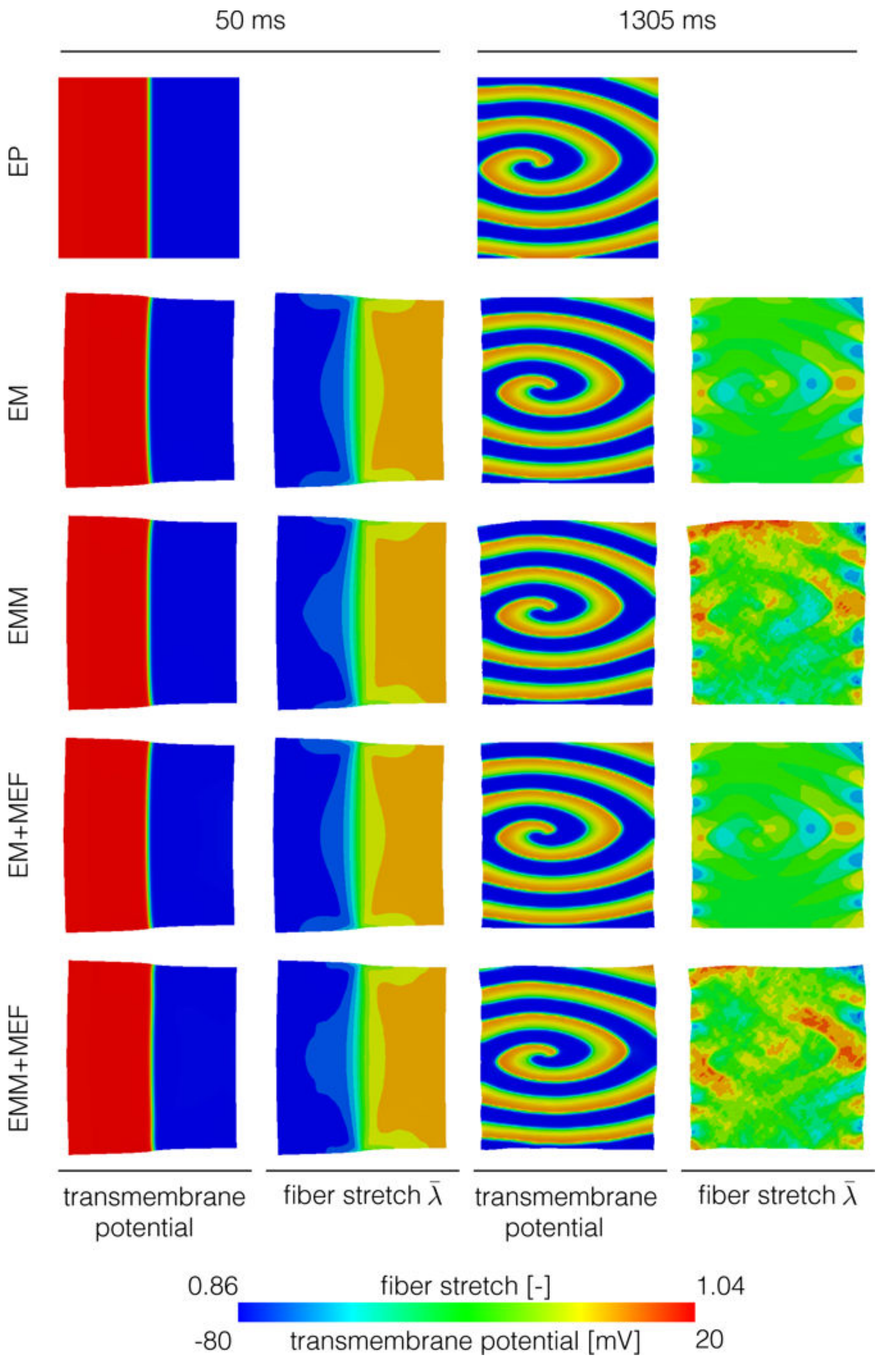

Figure 6.

Planar wave propagation (left) and spiral wave (right) for all cases considered. The inertial effect creates tensile fiber stretch during the spiral wave stage that are not present when mass is not considered.

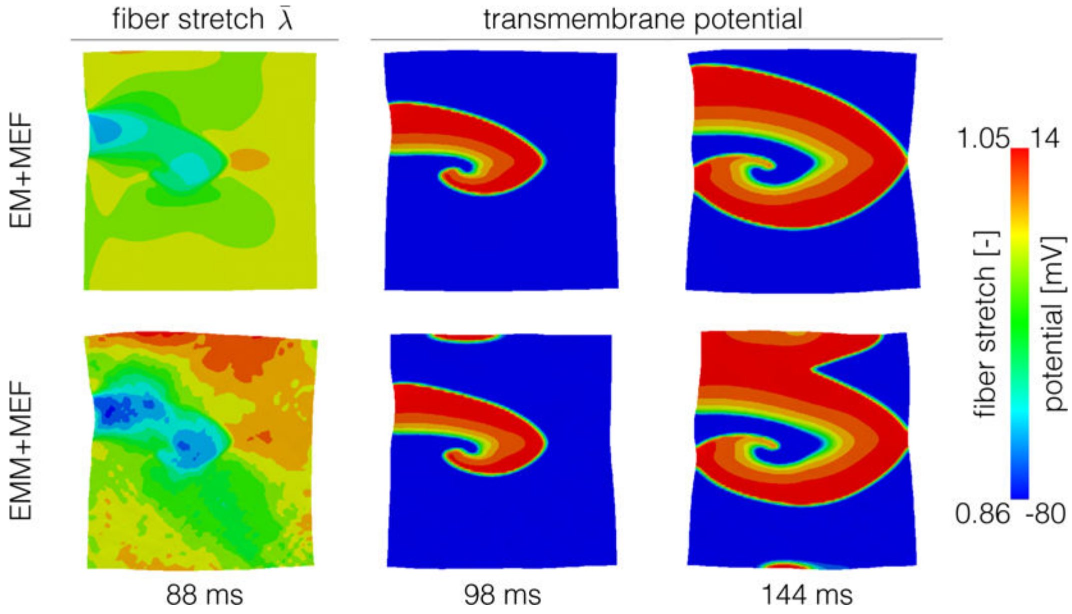

Figure 7.

Effect of mechano-electrical feedback on spiral waves. When we include mass (lower row), there are regions of high tensile fiber stretch that create mechano-electrical currents. These currents later translate into secondary activation fronts at times 98 ms and 144 ms. This effect is not present when we neglect inertia (upper row).

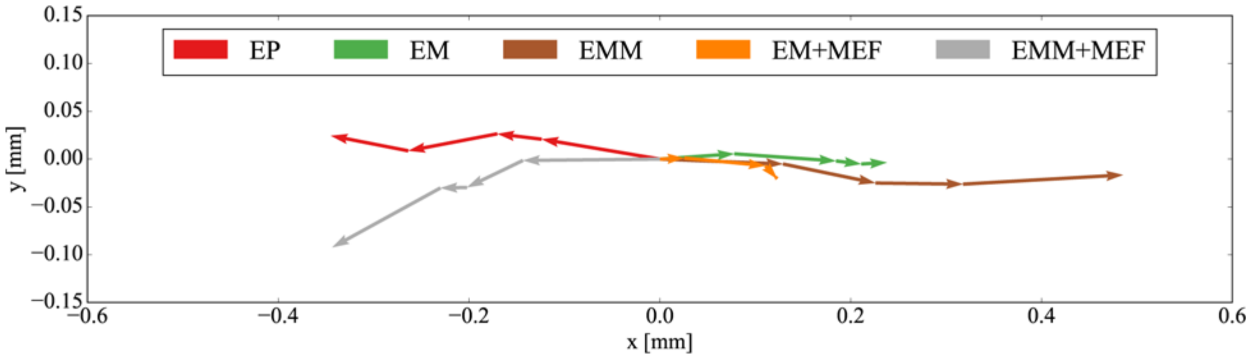

Figure 8.

Trajectories of the spiral wave center. We observe that cases with mecho-electrical feedback tend to have shorter trajectories and cases with mass tend to have longer trajectories.

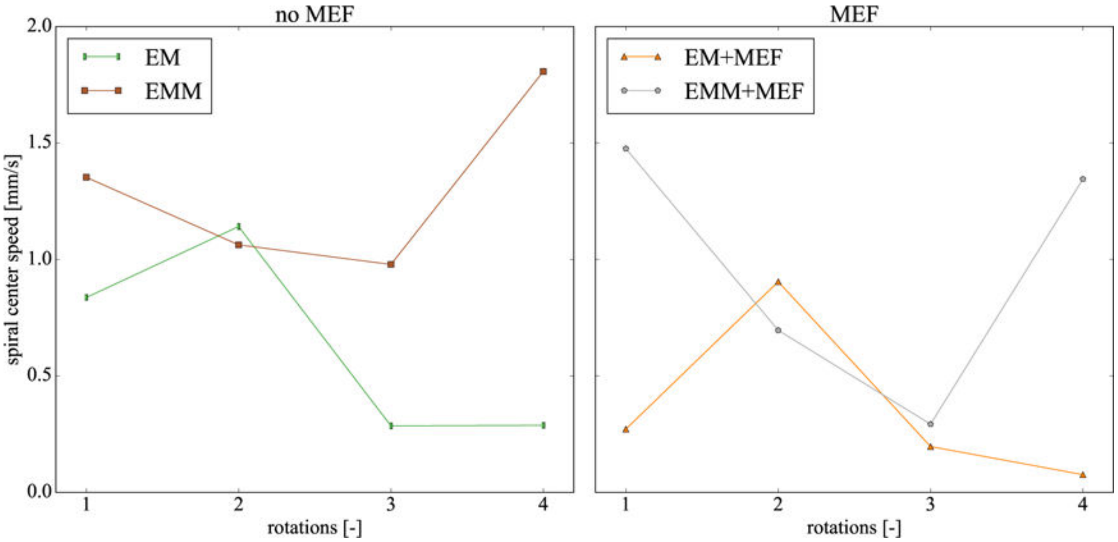

Figure 9.

Speed of spiral wave center. The cases with mass have greater speeds for most rotations, particularly towards the end. This trend suggest that the spiral would continue drifting, while in the cases without mass, the spiral would stabilize in one position.

Table 1

Cases considered in the numerical study. The ✓symbol marks the components present in each model.

case/component	Electrophysiology	Mechanics	Mass	Mechano-electrical feedback
EP	✓			
EM	✓	✓		
EMM	✓	✓	✓	
EM+MEF	✓	✓		✓
EMM+MEF	✓	✓	✓	✓

Table 2

Model parameters used in all simulations.

electrical			
conduction	$d^{\text{iso}} = 0.0952\ \text{mm}^2/\text{ms}$	$d^{\text{ani}} = 0.03\ \text{mm}^2/\text{ms}$	[42]
excitation	$\alpha = 0.05$	$\gamma = 0.002$	[27]
	$c_1 = 52$	$c_1 = 8$	[34]
	$\mu_1 = 0.1$	$\mu_2 = 0.3$	[27]
	$b = 0.35$		
mechanical			
passive	$\rho_0 = 1.1\ \text{g/cm}^3$	$\lambda = 100$ kPa	
	$\mu = 3.91$ kPa	$\eta = 4.02$ kPa	
active	$k_T = 0.015$ kPa/mV	$\Phi_{\text{r}} = -80$ mV	
coupling			
activation	$\varepsilon_0 = 0.01/\text{mV}$	$\varepsilon_\infty = 1/\text{mV}$	[18]
	$\xi = 0.5/\text{mV}$	$\overline{\Phi} = -75\text{mV}$	[18]
MEF	$G_{\text{s}} = 20$	$\Phi_{\text{s}} = 0.6$	[54]

Table 3

Results from the conduction velocity study.

	$\Delta x = 0.1$ [mm]			$\Delta x = 0.25$ [mm]			$\Delta x = 0.5$ [mm]		
Δt [ms]	**0.005**	**0.01**	**0.05**	**0.005**	**0.01**	**0.05**	**0.005**	**0.01**	**0.05**
EP	0.394	0.395	0.401	0.389	0.390	0.397	0.374	0.375	0.382
EM	0.408	0.409	0.416	0.404	0.404	0.411	0.389	0.390	0.397
EMM	0.409	0.410	0.417	0.404	0.405	0.412	0.390	0.391	0.398
EM+MEF	0.419	0.420	0.427	0.415	0.416	0.423	0.402	0.403	0.411
EMM+MEF	0.426	0.427	0.435	0.422	0.423	0.431	0.410	0.411	0.418

Table 4

Percentage differences in conduction velocity for the different models using $\Delta x = 0.1$ mm, $\Delta t = 0.005$ ms. The differences are calculated as (row - column)/row.

	EP	EM	EMM	EM+MEF	EMM+MEF
EP	–	3.62%	3.82%	6.31%	8.12%
EM	−3.49%	–	0.20%	2.60%	4.35%
EMM	−3.68%	−0.20%	–	2.40%	4.14%
EM+MEF	−5.94%	−2.54%	−2.34%	–	1.70%
EMM+MEF	−7.51%	−4.16%	−3.97%	−1.67%	–